THE PALISADE LAYER OF THE POXVIRUS CORE IS COMPOSED OF FLEXIBLE A10-TRIMERS

Jiasui Liu[1,*], Simon Corroyer-Dulmont[2,*], Vojtěch Pražák[3], Iskander Khusainov[1], Karola Bahrami[4,#], Sonja Welsch[5], Daven Vasishtan[6] , Agnieszka Obarska-Kosińska[1], Sigurdur R. Thorkelsson[2,##], Kay Grunewald[2,6,], Emmanuelle R. J. Quemin[2,7,**], Beata Turoňová[1,**], Jacomina Krijnse Locker[4,8**]**

[1] Max Planck Institute of Biophysics- Molecular sociology
Max-von-Laue Strasse 3, 60438 Frankfurt/Main, Germany

[2] Centre for Structural Systems Biology, Leibniz Institute of Virology, Hamburg, Germany

[3] University of Hamburg, Hamburg, Germany

[4] Paul Ehrlich Institute- Electron microscopy of pathogens
Paul Ehrlich Strasse 51-59, 63225 Langen, Germany

[5] Max Planck Institute of Biophysics- Electron Microscopy
Max-von-Laue Strasse 3, 60438 Frankfurt/Main, Germany

[6] Division of Structural Biology, Wellcome Centre for Human Genetics, University of Oxford, Oxford OX3 7BN, United Kingdom

[7] Department of Virology, Institute for Integrative Biology of the Cell (I2BC), CNRS UMR9198, Gif-sur-Yvette, France

[8] Justus Liebig university of Giessen, Giessen Germany

[#] Present address: University Clinic Frankfurt, Frankfurt am Main, Germany
[##] Present address: MRC Laboratory of Molecular Biology, Francis Crick Avenue, Cambridge, CB2 0QH, United Kingdom

[*] Joint first author
[**]Joint corresponding authors
kay.gruenewald@cssb-hamburg.de ; emmanuelle.quemin@i2bc.paris-saclay.fr;
beata.turonova@biophys.mpg.de; jacomina.krijnselocker@pei.de

Abstract

Although vaccinia virus (VACV) is the best studied poxvirus, the structure of the mature virus (MV) remains poorly understood. Its asymmetric shape, size and compactness poses a major challenge for electron microscopy (EM) analysis, including cryoEM. Sub-viral particles, in particular membrane-free viral cores, may overcome these limitations. We compare cores obtained by detergent-stripping MVs with cores in the cellular cytoplasm, early in infection. By combining cryo-electron tomography (cryoET), subtomogram averaging (STA) and AlphaFold2 (AF2), abundant core-structures are analyzed, focusing on the prominent palisade layer located on the core surface. On detergent-stripped cores, the palisade is composed of densely packed trimers of the major core protein A10. They display a random order on the core surface and classification of the trimers indicate structural flexibility. On cytoplasmic cores A10 is organized in a similar manner, indicating that the structures obtained *in vitro* are physiologically relevant. CryoET and STA also uncover unexpected details of the layers beneath the palisade both on *in vitro* and *in situ* cores, that are compared to AF2 structure predictions of known VACV core-associated proteins. Altogether, our data identify for the first time the structure and molecular composition of the palisade units. The results are discussed in the context of the VACV replicative cycle, the assembly and disassembly of the infectious MV.

Introduction

The recent emergence of monkeypox virus infections in Europe and North America has rekindled an interest in poxviruses. The prototype of the poxviruses, vaccinia virus (VACV), was used previously as a live vaccine to eradicate smallpox and has been studied extensively, biochemically, genetically, and morphologically (reviewed in by B. Moss [1]). However, despite extensive investigation, questions remain about the biogenesis and structure of the mature virion (MV)[2].

The infectious mature virion (MV) is a quasi-brick shaped particle measuring roughly 250x350x200 nm. It is composed of an oval or brick-shaped core enclosing the viral genome as well as the machinery required for transcription early in infection. This core is surrounded by a lipid bilayer acquired during assembly; two so-called lateral bodies are located on the elongated sides of the core-brick, underneath the viral membrane [3]. The MV is composed of roughly 200 proteins. Treatment of MVs with a non-ionic detergent and a reducing-agent results in a membrane-free, stable, core [4], which is widely used to discriminate viral proteins associated with the membrane and the core. Thus, the membrane-free core is known to be composed of at least five abundant proteins; gene products of A3, A4, A10, L4 and F17 [2]. With the exception of F17 these proteins are also associated with the incoming, cytoplasmic core, early in infection [5].

Although the MV has been studied extensively by electron microscopy (EM), including cryoEM, its precise structure remains elusive. Structural analyses are hampered in particular by the compactness of the virion and its asymmetric shape. Thus, sub-viral structures have also been studied, in particular the membrane-free and detergent-stripped core, by classical negative staining EM [6], [7] and by cryoEM [8]. Such cores display a dense spike-like layer, the so-called palisade, on their surface. The cryoEM data by the team of Jacques Dubochet proposed that the palisade units are hollow tubes, roughly 20nm long and 10nm in diameter, which are tightly packed on the core surface in a disordered and ordered way, forming a hexagonal lattice with a 9.7 nm spacing. Analyzing the intact MV by cryo-electron tomography (cryoET), Cyrklaff et al. concluded that the palisade-units on the core surface were 8nm in length and 5nm in diameter and arranged in hexagonal lattices [3]. A recent publication studying VACV assembly by cryoET in the periphery of infected cells, also proposed an ordered arrangement of the palisade on fully assembled virions. The model in this study displayed the palisade as trimeric pillars with projecting lobes that mediate interpillar contacts [9].

Although the major proteins associated with membrane-free cores are known, it is unclear which of these proteins make up its prominent features, such as the core wall and the prominent palisade[2]. Wilton et al., using antibody labeling, suggested that the palisade is made up by the gene product of A3 [7].

In the present study we apply cryoET and subtomogram averaging (STA) to study the structure and molecular composition of the palisade both *in vitro* and *in situ.* From the *in vitro* data we obtain a structure of the palisade units at less than 7.7Å resolution. The latter faithfully represents the structure of the palisade *in situ*, on the surface of the incoming core early in infection. We apply AlphaFold2 [10] to predict the 3D structure of the five major core proteins; by flexible fitting of the predicted structure of the gene product of A10 into the obtained map, we show that the palisade units are made up of trimers of this core protein. The relevance of these data, including additional features we observe in our cryo-tomograms, are discussed with respect to the biology of poxvirus infection.

Results

Sample preparation of Vaccinia virus cores for cryo electron tomography

For structural analysis of the viral core of Vaccinia virus by cryo electron tomography (cryoET), we first optimized sample preparation to obtain intact cores *in vitro*. Based on previous studies, short incubation with 0.1% NP-40 and 10 mM freshly prepared dithiothreitol (DTT) diluted in 50 mM Tris-Cl pH 8.5 appeared to be the optimal conditions. These freshly prepared cores are structurally intact and remain associated with lateral bodies, while storing them at -80°C results in a considerable number of broken cores. Sonication prior to vitrification is essential to obtain a sufficient number of individual cores on cryoEM grids. Vitrified samples are inspected in a Titan Krios G4 (Thermo Scientific) TEM and areas containing single cores located in the holes of the grids selected for cryoET. In total, 34 tilt series were acquired and reconstructed into tomograms, yielding 50 cores that were used for further analysis. For comparison, supplemental Figure S1 and Movie S1 display a typical MV from purified preparation, exemplifying the complexity of its structure.

The cores of Vaccinia virus prepared *in vitro* display three layers

Reconstructed tomograms of the cores prepared *in vitro* confirm the overall organization observed previously (Fig.1, Movie S2) [8]. The core has a brick-like shape with average dimensions of 200 nm by 320 nm by 200 nm. The inside of the core is sparsely filled with electron-densities possibly representing the viral genome in complex with DNA-binding proteins or the transcription machinery packaged during assembly [11]. It is enclosed by at least three layers (Fig. 1b). The most prominent is the outer palisade layer composed of protrusions with a tube-like shape of ~11 nm in height and diameter of 8 nm (Fig. 1b). Being subunits of the palisade, we will refer to these tubular structures as stakes throughout this study. The stakes do not form a regular lattice (Fig. 1b, d) in contrast to what has been described previously [8], [9], [12]. At their top part, the stakes are often connected to their neighbors with thin threats (Fig. 1d). The ring structure reported in [9] is integrated into the palisade (Fig 1c). Below the palisade is the middle layer, the inner core wall with a thickness of 4-5 nm (Fig. 1e). From the side, the layer resembles a lipid bilayer (Fig. 1e), however it appears as stripes when viewed from the top with very weak perpendicular connections between the stripes. The most inner layer is roughly 3 nm below the inner core wall and has a thickness of less than 2 nm. The content of this layer appears irregular within each core: it can contain 1 or several rows (Fig. 1b, f) and is sometimes even absent. Strong densities are occasionally found to be connected to the top of the stakes (Fig. 1c). Consistent with previous data and the gentle sample preparation procedure we used, these *in vitro* cores also contain two large blob-like structures on both sides: the lateral bodies. Our dataset confirms that the lateral bodies are amorphous and reveal some connection sites linking them to the spikes of the palisade layer (Fig. 1b).

AlphaFold2 predictions of major core proteins

AF2 [10] was used to predict the 3D structure of five viral proteins known to be abundant in fractions of cores prepared *in vitro* [4]. These are the gene products of A3, A4, A10, and L4 and the lateral body protein F17 [5]. The predictions were computed for various assemblies, from monomers to hexamers and different combinations of the proteins (for full list, see Table S1.1 to S1.3). Based on the confidence scores, A3, A10, and L4 were found to form ordered structures for all tested symmetries, while A4 and F17 are mostly disordered (Fig. S2a).

The palisade is composed of trimers of the major core protein A10

The initial low-resolution structure, obtained from the alignment of 400 manually picked stakes, displays a tube-like shape with a diameter of 9 nm and a length of 11.5 nm (Fig. S3c). From the AF2 predictions of the major core proteins (Fig. S2a), a trimer of A10 fits in shape and size to this first average (Fig. S3c). We used the AF2-predicted A10 trimer (Fig. 2a) as an initial reference to localize the stakes on all segmented cores using the oversampling approach (see Methods for more details). To limit potential template bias, the initial reference for the subsequent alignment was created using only the positions, not the orientations found during the localization (Fig. S2f). For the classification, we followed the protocol from [13]. First, we obtained 20 different *de novo* classes as potential candidates for further classification. 8 classes stand out with significant structural differences in the central parts of the stake (Fig. S4a, b), while the remaining 12 classes are variations with minor differences in protomer positions and orientations, confirming the inherent flexibility of the stake arrangements. Following the classification protocol, the 8 classes were used as starting references for several independent classification runs (Fig. S4b). These revealed classes with distinct features located within the central part of the stake. Specifically, they were characterized by the absence or presence of densities connecting the three protomers across the inner central region (Fig. S4b), and were assigned as hollow and connected trimers, respectively (Fig. 2b). Interestingly, mapping the classes back to the tomograms shows that there is no preferential clustering or location of the different classes on the core surface (Fig. S4d).The majority of classes form hollow trimers and have minor differences in orientation relative to the each other (Fig. S4b). The measured overall resolution of the best hollow and connected classes reached 7.7Å and 7.6Å, respectively.

Obtained STA structures indeed correspond to the trimers of A10 protein as suggested by the result of systematic fitting and subsequent molecular dynamics flexible fitting of the AF2-predicted model of A10 trimer into STA map of the hollow trimer (Fig. S5a-d). This is supported by visual inspection of the secondary structures (Fig. S5e), and the model-to-map cross-correlation analysis (Fig. S5f). Notably, domain 3, which was predicted with the least confidence by AF2, also showed the lowest cross-correlation with the map (Fig. S5f). This, together with the high variability of domain 3 in STA structures, may suggest its role beyond forming the structural scaffold.

The scaffold of an A10 trimer and the major contact sites between its protomers were addressed by fitting of the AF2 model of the A10 trimer into the hollow and connected structures (Fig. 2e-h). While the hollow trimer is supported by a relatively weak hydrophobic interactions between Leu 10 and Leu 13 located near domain 3 (Fig. 2f, circular subpanel), in the connected trimer, protomers form three intermolecular beta sheets stabilized by electrostatic interactions between Asn 101 located in the flexible loop in the central channel of the trimer (Fig 2h).

The palisade is an integral part of the incoming core during entry in cells

To exclude potential artifacts from the preparation of cores *in vitro*, we compare the structure of the palisade observed on cores *in vitro* and *in situ*. Tomograms of cores found in the cytoplasm of host cells early in infection shortly after entry have also been acquired. In brief, HeLa cells grown on grids are plunge-frozen at 30 minutes post-infection without prior chemical fixation and prepared by focused ion beam (FIB)-milling (see Materials and Methods). 15 tilt series were acquired containing cytoplasmic cores and after tomogram reconstruction, 5 incoming cores were used for averaging of the palisade trimer as described above for the *in vitro* cores (Fig. 4a).

The overall architecture of the incoming cores observed *in situ* is very similar to the cores prepared *in vitro* (Fig. 1 and 3,Movie S3). The outer layer represents the prominent palisade (Fig. 3b) while the middle layer has a stripy appearance as highlighted above (Fig. 3a, c). The cytoplasmic cores are devoid of lateral bodies, known to dissociate immediately after entry and membrane fusion [5], [13]. The electron-dense layer found lining the core wall in the samples prepared *in vitro* is not seen in cytoplasmic cores (Fig. 3a). Instead, the central part of the core is homogeneously filled with filaments likely representing decondensed DNA, as described before (Fig.3a)[12]. A remarkable feature that was not observed *in vitro,* is the presence of strands attached to the palisade that have been previously reported by Hernandez et al. [9] and could be early transcripts leaving the core (Fig. 3d). Finally, the ring-like structures located between the palisade stakes found in *in vitro* cores (Fig. 1c), are also observed on the cytoplasmic cores (Fig. 3b).

Comparison of the palisade spike *in vitro* and *in situ*

While finding and imaging incoming cores directly in infected cells remains challenging, the structure of the palisade stalks from these *in situ* data was resolved to 14 Å even with a lower number of events. This is sufficient to conclude that the size and shape of the palisade from *in situ* cores is consistent with the *in vitro* one when compared at the same resolution (Fig. 4a). We further tested whether the stakes on intracellular cores are closer to the AF2 prediction model or our *in vitro* model by running alignment of the *in situ* data against both models. The constrained cross correlation scores were higher for the in vitro-based model than to the AF2 prediction of A10 trimer giving us confidence that we observe a physiologically relevant conformation of the stakes after classification of the subtomogram averages (Fig. 2).

To further confirm the visual similarity between the *in vitro* and *in situ* cores, nearest-neighbor analysis was performed. The average distance between neighboring stakes is 9 nm for both datasets and the analysis of the normalized nearest neighbor position shows a similar trend (Fig. 4,b). This analysis confirms the irregular arrangements of the lattice *in situ*, since there is no visible positional preference of the nearest neighbors. The average number of stakes per core is 2690 for the *in vitro* data. Given that the *in situ* cores are not fully contained within the tomograms acquired on lamellae, we calculated an average stake density on the core surface by dividing the surface area of the core segmentation by the summed areas stakes projections on the core surface. . There is on average 1.2 number of stakes per 1Å^2 surface for *in situ* cores and 1.3 for *in vitro* cores.

Discussion

Among the first steps of the replicative cycle of VACV is the release of the viral core into the cytoplasm to initiate infection. This core has been studied to quite some extend, morphologically and biochemically, but the molecular composition of its sub-unit has remained elusive [5]. Cores can also be prepared from detergent-stripped virus, which facilitated previous studies [8] and our present analysis, combining cryoET, STA and AF2. We show that the prominent palisade layer is composed of trimers of the gene product of A10. A10 is an abundant VACV core protein that is essential for the formation of the MV [14]; it is synthesized as a 110kDa precursor that is cleaved to a 65kDa form during virion maturation [15]. This maturation step is accompanied by the formation of the typical brick-shaped core, displaying the palisade on its surface. As described before, the palisade units appear as trimers forming hollow tubes [8], [9]. Our study identified more than twenty different classes displaying minor differences in protomers orientations. Among those two global classes can be distinguished, one class presents an open, hollow, central part, whereas the other displays densities that connect the protomers across the center. This together confirms the structural flexibility that can be observed in tomograms where stakes appear to adopt slightly different shapes (Fig 1). The class with the best resolved features and highest resolution was used for model fitting with the AF2 prediction used as a starting model. It generally fitted the cryoET structure well, although the central channel of the trimer of the native structure appeared to be more open. Most importantly, we show that the structure of the stakes on detergent-stripped virions is similar to the one on incoming core, making us confident that it is physiological relevant. In fact, the *in vitro* and *in situ* structures fitted each other better than the one predicted by AF2.

The different classes are randomly distributed on the surface of the core without any clustering at specific locations such as the corners of the core. The stakes on both *in vitro* and *in situ* cores are randomly organized and display no specific pattern as shown by nearest neighbor analysis. This seems to contradict previous data, proposing that the palisade shows both unorganized regions as well as patches with a hexagonal arrangement [3]. The difference can be explained by the use of different analysis for identifying hexagonal patterns. Alternatively, the palisade may more organized on the fully assembled infectious MV [3], [9] whereas it displays no obvious order on intermediates of disassembly, such as membrane-free cores.

The core is known to contain at least 5 abundant protein (see introduction), 4 of them are among the most abundant proteins of the MV, the gene products of A3, A10, A4 and F17 [16], implying important structural roles. F17, a 11kDa protein, is known to be part of the lateral bodies. These may remain attached to cores prepared by gentle detergent-stripping as in this study, but dissociates from the core immediately after entry [5]. AF2 predicts F17 to be generally unordered, which may fit the amorphous appearance of the lateral bodies observed before and in this study. Although the tomograms allow us to draw the model as in figure 1a, attempts to fit the AF2 predictions of other major core proteins within the structures obtained were unsuccessful until now. Because these proteins are known to be part of viral core, the lack of high-confidence response in the tomograms likely reflect discrepancies between the AF2 predictions and the experimental data at high resolution. The high-confidence TM relies on high-resolution information, especially in case of small templates or templates without distinct shape such as predictions for monomers of A3 and L4. The accompanying manuscript predicts the A3 to constitute the core wall below the palisade, a prediction that is consistent with immuno-labeling experiments on cytoplasmic cores [5]. Indeed, based on the AF2 prediction the monomer or dimer of A3 could fit size-wise into the core wall. In addition, it displays strong negative charges on part of the surface that would allow it to connect to the base of the A10 trimer which is positively charged. The location of A4, a 39kDa protein, remains unknown at this stage; again, previous immuno-labeling experiments on cytoplasmic cores would place this protein on the core surface. Indeed, our tomograms occasionally suggested the presence of an additional density on top of the palisade, but its characterization requires further analysis.

The identification of the molecular and structural composition of the palisade questions its function, elusive until this date. Its abundance suggests it to shape the core it into its characteristic form during virion maturation, linking the core to the viral membrane and the lateral bodies. Indeed, we detected direct interactions between palisade units and the lateral bodies as described recently [9]. Accordingly, the palisade could fulfill a scaffolding function similar to the gene product of D13 during membrane assembly as recently suggested [9]. Being an abundant and flexible protein, we speculate the stakes to have additional functions related to the early replicative cycle, when the palisade is prominently exposed on the core surface. The cytoplasmic core is known to interact with microtubules [17] and the palisade stakes could mediate this interaction. The rings on the core surface, observed before [9] and in the accompanying study are typically surrounded by A10-trimers. The latter might support, stabilize the rings or contribute to their typical ring-like structure. The subsequent step of the early infection is the uncoating of the DNA-genome and its release into the cytoplasm for replication. Images documenting this event suggest that genome-release occurs by a single and distinct break in the core wall [5], [12]. A distinct subset of A10 trimers could facilitate this opening, undergoing rearrangements that locally modifies the palisade layer and destabilizes the underlying core wall, for release of the viral DNA.

Altogether by combining cryoET, STA and AF2 we have identified the composition of the VACV palisade. The A10-trimer is an abundant and highly flexible protein, with the potential to fulfill multiple functions during the VACV assembly and disassembly.

Acknowledgments

We thank Sylvia Panitz and Regina Eberle, microscopy facility Paul Ehrlich Institute, for excellent technical assistance. We also acknowledge support by Cornelia Cazey, Ulrike Laugks, and Carolin Seuring, for access to the Cryo-EM multi-user facility at CSSB and providing time for sample preparation, screening, and data collection; Wolfgang Lugmayr for help and support in using the CSSB partition on the DESY computer cluster for cryo-EM data processing. Part of this work was performed at the Cryo-EM multi-user Facility at CSSB, headed by K.G. and supported by the UHH and DFG (grants INST 152/772-1, 774-1, 775-1 and 776-1). In the framework of this project, E.R.J.Q. was supported by an individual fellowship from the Alexander von Humboldt Foundation and a Klaus Tschira Boost Fund. JKL is supported by the excellence cluster Loewe DRUID of the state Hesse, project E7-P. JL is supported by DFG (project 515013236).

Contributions

JL, SCD, VP, IK, DV, AOK, SRT, BT did the image processing and modeling. SCD, KB, SW sample preparation and image acquisition. KG, ERJQ, BT, JKL designed the experiments, ERJQ, BT and JKL wrote the manuscript.

Declaration of Competing Interest

The authors declare that they have no known competing interests.

Data availability

The electron microscopy density maps of the A10 trimers have been deposited in the Electron Microscopy Data Bank under accession codes: EMD-XXXX, EMD-YYYY, EMD-ZZZZ (loose and tight conformation from the *in vitro* dataset, trimer from the *in situ* data). The raw tilt series of the in vitro dataset together with representative tomograms from both *in vitro* and *in situ* datasets were deposited at EMPIAR- QQQQ. The python scripts developed for core picking and contextual analysis will be publicly available on github at the time of the publication.

Materials and Methods

Mature virions

Sample preparation. Mature virions (MV) of VACV strain Western Reserve (WR) were purified as previously described [8]. The preparation was sonicated 2x30 seconds in a waterbath sonicator prior to be mixed in a 1:1 ratio with 5 nm gold fiducials (UMC Utrecht). This solution was then added to Quantifoil™ 200 mesh R2/2 copper grids right before plunge freezing into liquid ethane/propane cooled to liquid nitrogen temperature using a Vitrobot Mark4 (ThermoFisher Scientific) after blotting for 3 seconds at 4°C.

Data collection. At the Cryo-EM multi-user facility at CSSB, the grids were imaged using a Titan Krios G3 operated at 300 kV (ThermoFisher Scientific) and equipped with a K3 camera as well as a BioQuantum post-column energy filter (Gatan). Grids were screened and tilt series acquired using SerialEM [18]. The low-dose mode was setup to achieve a dose of ~15 e-/pixel/sec on the detector directly on the sample with a 70 µm objective aperture and a 20 eV energy slit width. Tilt series were collected with the dose-symmetric tilt scheme [18] over a +/-60 degrees tilt range with a 3 degree increment step. Movie frames were recorded in electron counting mode with a pixel size of 1.372 Å, a target defocus of -3 µm and a total dose of 1.5 e-/Å^2 over 10 frames, resulting in a total dose of ~80 e-/Å^2 for each tilt series.

Data processing. Tomograms were processed within eTomo (IMOD 4.11 package) [19]. Prior the reconstruction, the tilt series were aligned using the fiducial-based alignment and dose-weighting was applied to remove the damaging frequencies. The tomogram reconstruction was done with 3D-CTF correction and SIRT-like filter equivalent to 7 iterations.

Cryo electron tomography of viral cores prepared *in vitro*

***Sample preparation*.** Purified VACV MVs were diluted in 50 mM TrisCl, pH 8.5 and mixed with an equal volume of 0.2% Nonidet P-40 and 20 mM DTT diluted in Tris-CL. The mixture was sonicated 3 times for 1 minute in a waterbath sonicator and then incubated in a ThermoMixer (Eppendorf) for 30 minutes at 37°C and 500 rpm. The mixture was layered on a 36% (w/v) sucrose in 50 mM Tris, pH 8.5 and the cores pelleted in a table top centrifuge at 100,000 rpm. The sucrose was removed without disturbing the invisible pellet and last drops of sucrose drained by placing the tube top down for several minutes on Whatman paper. The pellet was then resuspended in 50 mM Tris-Cl, stored on ice before further processing.
For cryo electron tomography, the freshly prepared cores were water bath-sonicated for 3x1 min and mixed 4:1 (cores:gold) with 10 nm gold particles coupled to protein A (Cell Microscopy Core, Utrecht University). Quantifoil™ 200 mesh R2/2 copper grids were glow-discharged for 90 sec using a Pelco easiGlow device. Per sample, 3 µL were applied to freshly glow discharged grids and samples were plunge frozen in liquid ethane using a Vitrobot Mark4 (ThermoFisher Scientific) at 4°C and 100% relative humidity. Frozen samples were stored in liquid nitrogen until further use.

Data collection. Data were acquired using SerialEM software on a Titan Krios G4 transmission electron microscope (ThermoFisher Scientific), operated at 300kV and equipped with a CFEG, SelectrisX energy filter and Falcon4 direct electron detector, essentially as described in[19].

Grids were initially mapped at low magnification in 6x6 montages. Suitable grid square maps were collected with a bin 1 pixel size of 19.4 Å, 100 µm defocus, a 70 µm objective aperture and a 20 eV energy slit. SerialEM low-dose mode was setup to achieve ~7 e -/pixel/sec camera dose-rate with a 70 µm objective aperture and a 20 eV energy slit inserted. Tilt series data were collected in a dose-symmetric tilt scheme [18]over a +/-60 degrees tilt range with a 3 degrees tilt step in groups of 2 tilts. Tilt images were acquired in electron counting mode with a pixel size of 1.577 Å and a total dose of 3.0 to 3.1 e-/Å2 over 10 frames, resulting in a total dose of ~125 e-/Å2 per tilt series.

For tilt series acquisition of *in situ* cores in lamella of infected HeLa cells, grids were imaged using a Titan Krios G3 operated at 300 kV (ThermoFisher), equipped with a K3 camera and BioQuantum post-column energy filter (Gatan). Data were acquired using SerialEM: first grids were mapped using low magnification to localize the lamellae. Mapped grids were pre-tilted to the angle used during milling (specific for each lamella between 7 and 10 degrees) , which was the starting angle for tilt series acquisition. SerialEM low-dose mode was setup to achieve ~15 e -/pixel/sec camera on lamella with a 70 µm objective aperture and a 20 eV energy slit inserted. Tilt series data were collected in a dose-symmetric tilt scheme (Hagen et al, 2017) over a +/-60 degrees tilt range around the starting angle with a 3 degrees tilt step. Tilt images were acquired in electron counting mode with a pixel size of 2.653 Å, a target defocus of -5µm and a total dose of 4.5 e-/Å2 over ten frames, resulting in a total dose of ~200 e-/Å2 per tilt series.

Cryo electron tomography of viral cores *in situ*

Sample preparation. To image cores *in situ*, HeLa cells were grown overnight on Au/Au, R1.2/1.3, 200 mesh grids (Quantifoil) at 37°C and 5% CO_2. Cells were placed in serum-free DMEM high-glucose medium (Gibco) and virus (WR strain with A3 protein tagged with YFP, kindly provided to us by Michael Way, The Francis Crick Institute, UK) bound for 45 minutes at RT followed by 30 minutes at 37°C for virus entry. Grids were plunge-frozen in a Leica GP2 (blot position: 44 and 4.4; blotting time: 6 seconds; chamber set to 37°C and 80% humidity) and lamellae prepared in an Aquilos 2 (ThermoFisher Scientific). This dual beam scanning electron microscope is equipped with focused ion beam (Gallium) and operated by associated software Maps and AutoTEM. Sample preparation, milling and polishing steps were done automatically using AutoTEM with a milling angle target of 8 degrees (2 degrees of tolerance) and a final lamella thickness set to 120 nm.

Data collection. For tilt series acquisition of *in situ* cores observed in lamella of infected HeLa cells, grids were imaged using a Titan Krios G3 operated at 300 kV (ThermoFisher Scientific), equipped with a K3 camera and BioQuantum post-column energy filter (Gatan). Grids were screened and data acquired using SerialEM. First, grids were mapped using low magnification to localize the lamellae. Mapped grids were pre-tilted to the angle used during milling (between 7 and 10 degrees, specific for each lamella), which was used as the starting angle for tilt series acquisition. SerialEM low-dose mode was setup to achieve ~15 e-/pixel/sec camera on lamella with a 70 µm objective aperture and a 20 eV energy slit inserted. Tilt series were collected using the dose-symmetric tilt scheme [18] over a +/-60 degrees tilt range around the starting angle with a 3 degrees tilt step. Tilt images were acquired in electron counting mode with a pixel size of 2.653 Å, a target defocus of -5 µm and a total dose of 4.5 e-/Å^2 over 10 frames, resulting in a total dose of ~200 e-/Å^2 for each tilt series.

Preprocessing and tomogram reconstruction

The defocus for each tilt series was estimated with CTFFind4 [20]. The tilt series were dose-weighted using the MATLAB script from [21]. Suboptimal projections or whole tilt series were removed from dataset, resulting in 34 tilt series. They were aligned using fiducial-based alignment within eTomo. The tomograms were reconstructed from 8x binned tilt-series using WBP with SIRT-like filter option. These tomograms were used only for picking of cores within Napari (see below). The unbinned tomograms were reconstructed using novaCTF [22] with phaseflip correction, astigmatism correction, and a 15nm slab size. These tomograms were binned 2x, 4x, and 8x using Fourier3D [23]. These 3D-CTF-corrected tomograms were used for subtomogram averaging (STA). For the complete parameter setup of individual steps see Table S2.

Subtomogram averaging (*in vitro*)

Created initial positions on the core surface. The cores were manually segmented by drawing contours around the cores in multiple layers of 8x binned tomograms in Napari. The layers were used to create the complete surface of the virions using the triangulation of the respective convex hulls. The resulting surfaces were then used to determine the starting position and orientations for STA (Fig S3a,b). Two sets of positions were produced for different purposes. The first set was generated for STA with an initial reference. For this set the surface was sampled at distance of 3.7 nm. The second set of positions was created specifically for resetting normal vector in *de novo* STA (see below). Surface for this set was sampled with distance of 1.2 nm.

Initial alignment. A total of 400 stakes were manually picked to generate the initial reference in novaSTA (Table S2). Subsequently, STA using all subtomograms was done in novaSTA [24] on 8x binned tomograms (Table S2). After the alignment, overlapping subtomograms were removed from further processing together with the subtomograms located near the carbon edge. The visual inspection of the aligned positions showed that the stakes are only partially covered and many subtomograms were aligned into the empty regions among them as these regions often resembled shape- and size-wise the stakes at this resolution. High cross-correlation threshold was used to select only subtomograms that were correctly located and obtained initial STA map from ~8000 subtomograms which gave us an estimate of the size and shape of the stakes (Fig S3c).

AlphaFold2 prediction. AlphaFold-Monomer version 2.2.0 [10] was used to generate models of four monomers of proteins A3, A4, A10, and L4 (Fig S2). AlphaFold-Multimer version 2.2.0 [25] was used to create multimers of these proteins as well as their combinations (see Table S1 for the full list). The AF2 parameters were set to default, except for the max_recycles parameter which was set to 12, to ensure convergence of the modeling. The models of the monomers were scored according to the predicted pLDDT score, while the models of protein complexes were scored using a combined ipTM (interface predicted TM-score) and pTM score (predicted TM-score), as returned by AF2 (Table S2).

***De novo* subtomogram averaging.** The overall shape of the initial STA map matched the AF2 prediction model of a trimer of A10 (Fig S3c). The AF2 model of the trimer was used as initial reference for STA on the oversampled surfaces. However, to utilize the high-resolution necessary to distinguish between the stakes and the regions among them the STA was done on 2x binned tomograms. The alignment resulted in correctly placed positions (Fig S3d) and a map resembling A10 trimer (Fig S3e). To avoid template bias, the orientations found during the STA were neglected. Instead, each subtomogram was assigned orientation based on its position on the surface. More precisely, the closest point from the second oversampled set was found and its normal vector was used to assign the cone angle of the subtomogram. The in-plane angle was assigned randomly. An STA average produced with the new orientation resembled featureless tube (Fig3f). This was used as a new starting reference for the STA that was done using STOPGAP [26]. The overview of the full parameter setup is in Table S2.

Classification. The visual inspection of tomograms suggested high flexibility of the stakes. The protocol from [27] was used to perform classification on the stakes using STOPGAP. In total 20 *de novo* initial references were created by choosing random subsets of particles (10 subset contained 10 000 particles, 10 subsets 5000 particles). Two independent STA runs of 15 iterations were done using simulated annealing for first 10 iterations (with temperature factor 10) and random search for the last 5 iterations. All twenty classes contained a trimer, however 8 classes contained distinct features separating them from others (Fig 4a). These 8 classes were used as initial references for 4 independent STA runs with random search. In total 10 iterations were enough for all the runs to stabilize (Fig 4c). Subsequently, the consistency cleaning was performed; only particles that ended in the same class for all 4 runs were kept, the rest was discarded. The remaining particles underwent 7 iterations of STA multiclass alignment (i.e., without the possibility to change the class). Class 6 (reported resolution 7.6Å) and class 7 (reported resolution 7.7Å) were used for further analysis as the tight trimer and the loose trimer, respectively. The 8 classes were mapped back to tomograms using ArtiaX plugin [28] for ChimeraX [29] to inspect possible clustering of classes. The model created using ArtiaX shows that there is no connection between the subtomogram class and its position on the cores.

Subtomogram averaging (*in situ*)

The STA on *in situ* data was performed in the same way as for the *in vitro* dataset with the exception of the initial alignment, which was skipped. Instead, after segmenting the cores, the STA was directly performed with AF2 model of A10 trimer. After the localization, the new orientations were assigned, followed by STA using STOPGAP. The trimer was resolved to the resolution of 13.4Å (Fig 4). The relatively low number of particles (~6000) prevented any attempts for classification. Table S2 contains all the parameters for the *in situ* STA.

Systematic fitting of AlphaFold models to cryo-EM maps

We followed the procedure from the work of Zimmerli et al. [30] to locate the AlphaFold models in cryo-EM map. The flexible chain at the N-terminus (Met 1 - Thr 9) and at the C-terminus (Ser 592 - Gly 614) of the model were removed due to no extra densities observed in that region. All the models were filtered to 9 Å, and the resulting simulated model maps were subsequently fitted into cryo-EM maps by global fitting as implemented in UCSF

Chimera [31] using scripts within Assembline [32]. The fitting was perform using 10,000 random initial placements, with at least 30% of the model map covered by the cryo-EM map. To evaluate the fit of each model, we used the cross-correlation about the mean (cam score), which was calculated using UCSF Chimera [31]. We assessed the statistical significance of each fitted model using a p-value derived from the cam scores. To obtain the p-values, we first transformed the cross-correlation scores to z-scores using Fisher's z-transform, computed two-sided p-values based on an empirical null distribution derived from all non-redundant fits, and corrected the p-values for multiple testing using the Benjamini-Hochberg procedure [33].

Flexible fitting and model analysis

To improve the fit of the A10 trimer, the molecular dynamics flexible fitting was performed using the model obtained by systematic fitting and the cryoET density map of the hollow trimer as inputs. The flexible fitting was performed in the web server of the Namdinator pipeline tool [34] in two sequential cycles with the following parameters: map resolution 12 Å, start temperature 500 K, final temperature 298 K, G-force scaling factor 0.3, minimization steps 5000, simulation steps 20000, phenix real space refinement cycles 0, implicit solvent excluded. The obtained model was subjected to phenix cryo-EM validation tool [35] to calculate model-to-map cross-correlation and the model-map Fourier shell correlation using default parameters and resolution set to 10 Å. The model to map fitting cross-correlation was calculated for the coordinates of one protomer and its corresponding density, as well as for individual domains of the protomer and their respective densities. All densities were segmented in ChimeraX [29] using the segger function [36] based on visual inspection.

For the analysis of the interprotomer contacts, specifically hydrophobic interactions between the alpha helixes Leu 10 – Leu 13 of domain 3 (Fig. 2f), and electrostatic interaction of the beta sheets Val 90 - Leu 92, Asn 96 - Ile 99, and Ile 104 - Ser 107 of domain 3 (Fig. 2h), the AF-predicted model was used. First, the trimer was fitted as a rigid body, then the corresponding regions were selected separately, and fitted as two individual rigid bodies into the densities of hollow and connected trimers. The molecular lipophilicity potential was calculated using the default fauchere method of the mlp function in ChimeraX based on MLPP program [37]. The electrostatic interactions between were calculated in ChimeraX of the Asn 101 residue of each protomer in the central channel of the trimer at the region of domain 2. The electrostatic potential of the beta-sheet-forming residues at the domain 2 region was calculated according to Coulomb's law using the Coulombic surface coloring tool in ChimeraX.

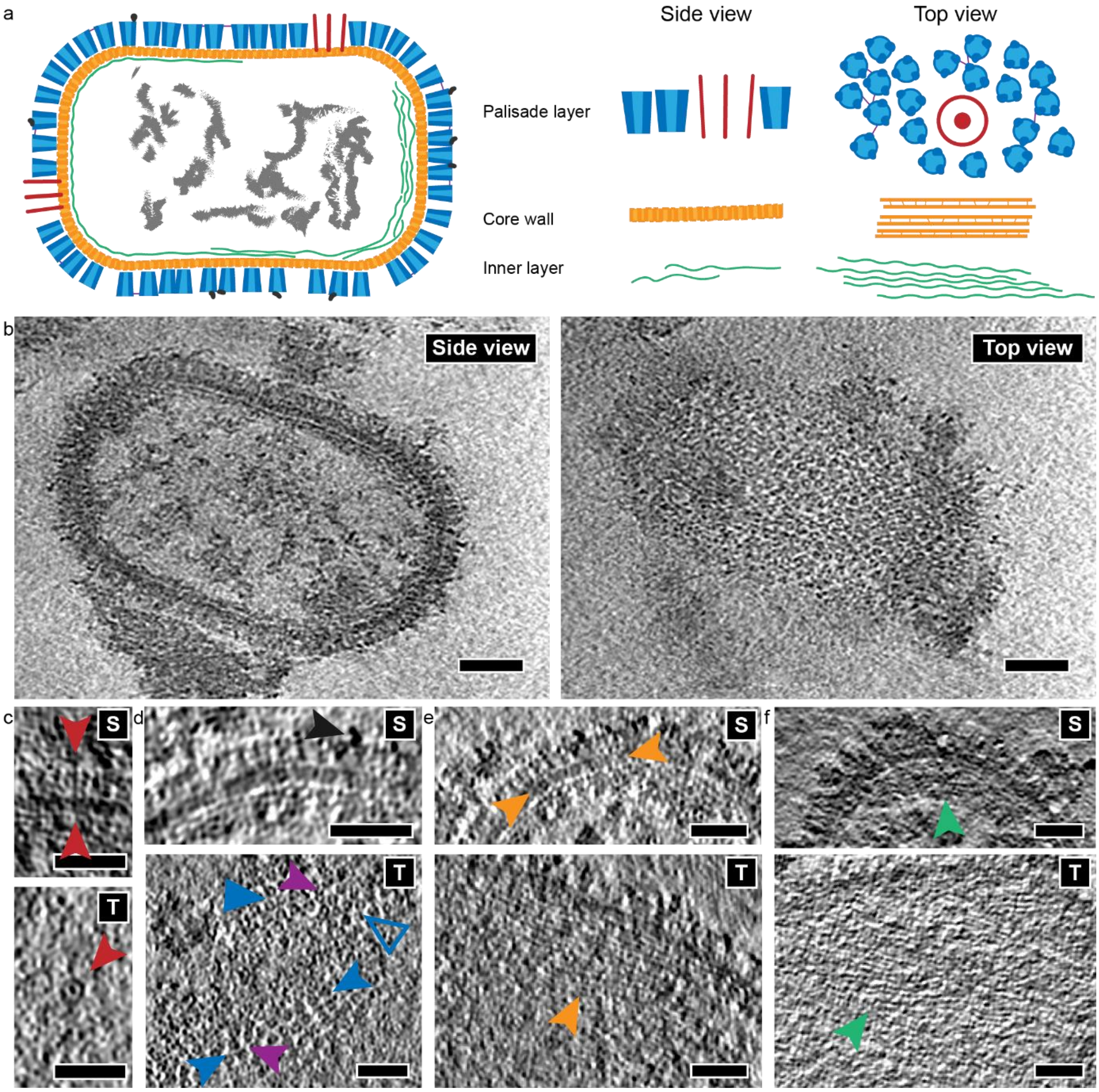

Figure 1: Appearance of the *in vitro* core. (a) Cartoon representation of the *in vitro* core based on the visual analysis of slices though a tomogram (Movie S2) (b) showing the middle of the core (left panel) and the surface of the palisade layer (right panel). The red structures, as circles from the top view, represent the ring-like structures. (b) Representative example of side (S) and top (T) view of the *in vitro* cores. The top layer displays the palisade of tube-like structures that have an irregular arrangement. The side view of the core reveals sparse density in the inner part of the core and the core wall consisting of three layers: the palisade (blue), the core wall (orange) and the most inner layer (green). (c-f) Close up of the three different layers surrounding the inner part of the core with the side and the top view. (c) A ring-like structure (red arrowhead). (d) Detail of the palisade layer at the surface of the core. The dark grey arrowhead points to the strong density occasionally observed on top of the palisade stakes. The blue filled triangle points to the hexagonal arrangement of the stakes while the hollow one to the similar arrangement, however consisting of eight, not seven stakes (including the middle one). The blue arrowheads point to the rails that are often formed on the palisade. The violet arrowheads mark the thin threads connecting the stakes. (e) Detail of the core wall layer, which has stripe-like pattern as seen from the top (orange

arrowheads). (f) Detail of the most inner layer from the side and top view (green arrowheads). Scale bars, 30 nm.

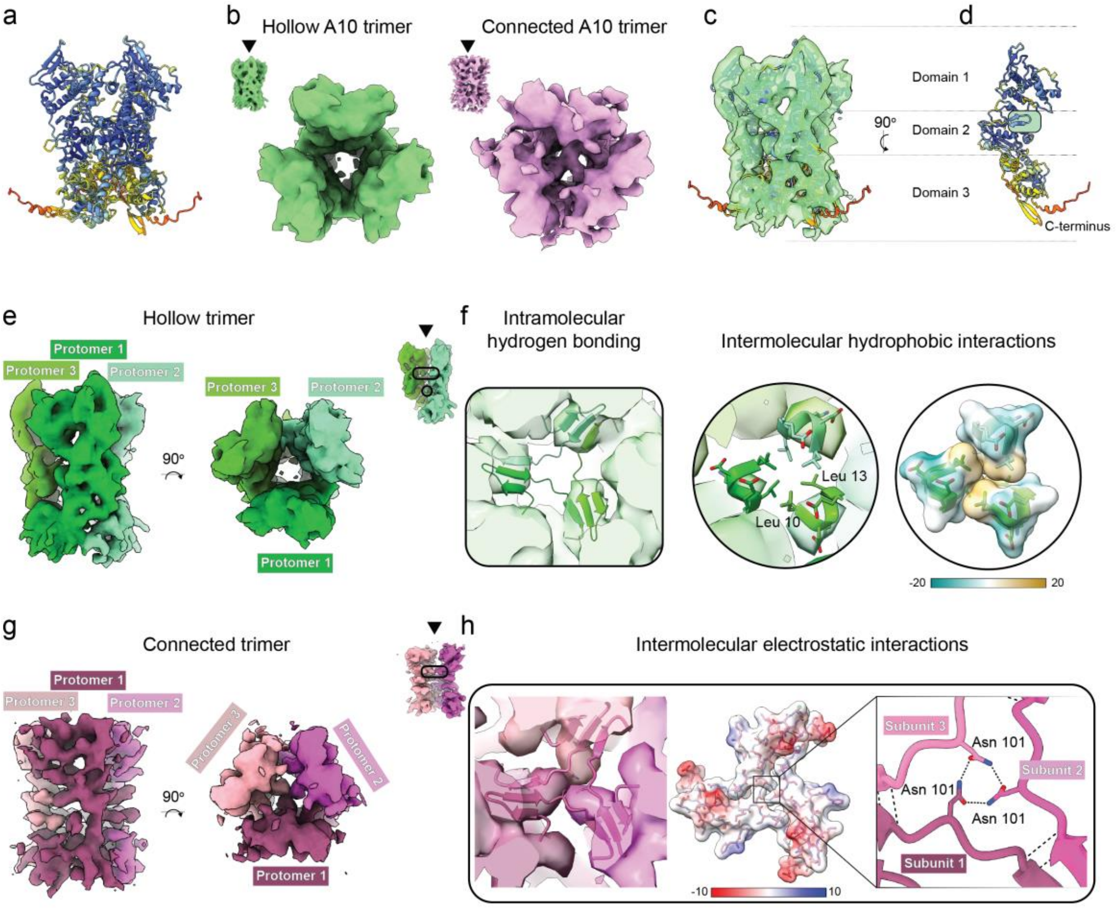

Figure 2: Classification and structural analysis of the palisade stalks made of A10 trimer. (a) AlphaFold2 prediction of A10 trimer colored by per-residue confidence score (pLDDT) between 0 and 100. Very high (pLDDT > 90, dark blue), confident (90 > pLDDT > 70, light blue), low (70 > pLDDT > 50, yellow), very low (pLDDT < 50, red). (b) Subtomogram averages (STA) of the two distinct A10 trimer classes, hollow (green) and connected (pink). (c) The AF2-predicted model of A10 trimer was rigid-body-fitted into the STA map of a hollow trimer. (d) The interface view of an individual protomer from the AF2-predicted A10 trimer. Coloring is same as in (a). The major interprotomer contact sites are highlighted with the green rectangle and green circle. (e) The STA density of the hollow trimer segmented into protomers colored in the shades of green. (f) The main contact points between protomers identified based on the fitting of AF2-predicted A10 trimer into STA density of the hollow trimer. The black rectangle shows the region for the interprotomer β sheets at the region of domain 2. The circles show the hydrophobic interface formed by the N-terminal residues Leu 10 and Leu 13 of each protomers. The hydrophobic surface is colored from dark cyan for the most hydrophylic to the dark gold for the most hydrophobic regions. The values correspond to the molecular lipophilicity potential calculated by the *fauchere* method of the mlp function in ChimeraX based on MLPP program. (g) The STA density of the connected trimer segmented into protomers colored in the shades of pink. (h) The main contact points between protomers identified based on the fitting of AF2-predicted A10 trimer into STA density of the connected trimer. The black rectangle shows the domain 2 region for the interprotomer beta sheets formed by two β strands of one protomer (Val 90 - Leu 92, and Asn 96 - Ile 99), and one β strand of the neighboring protomer (Ile 104 - Ser 107) is supported by electrostatic

interactions of the Asn 101 residue of each protomer in the central channel of the trimer at the region of domain 2. The middle subpanel represents electrostatic potential of atoms calculated according to Coulomb's law using Coulombic surface coloring tool in ChimeraX. The most negative potential colored in red, the most positive potential colored in blue.

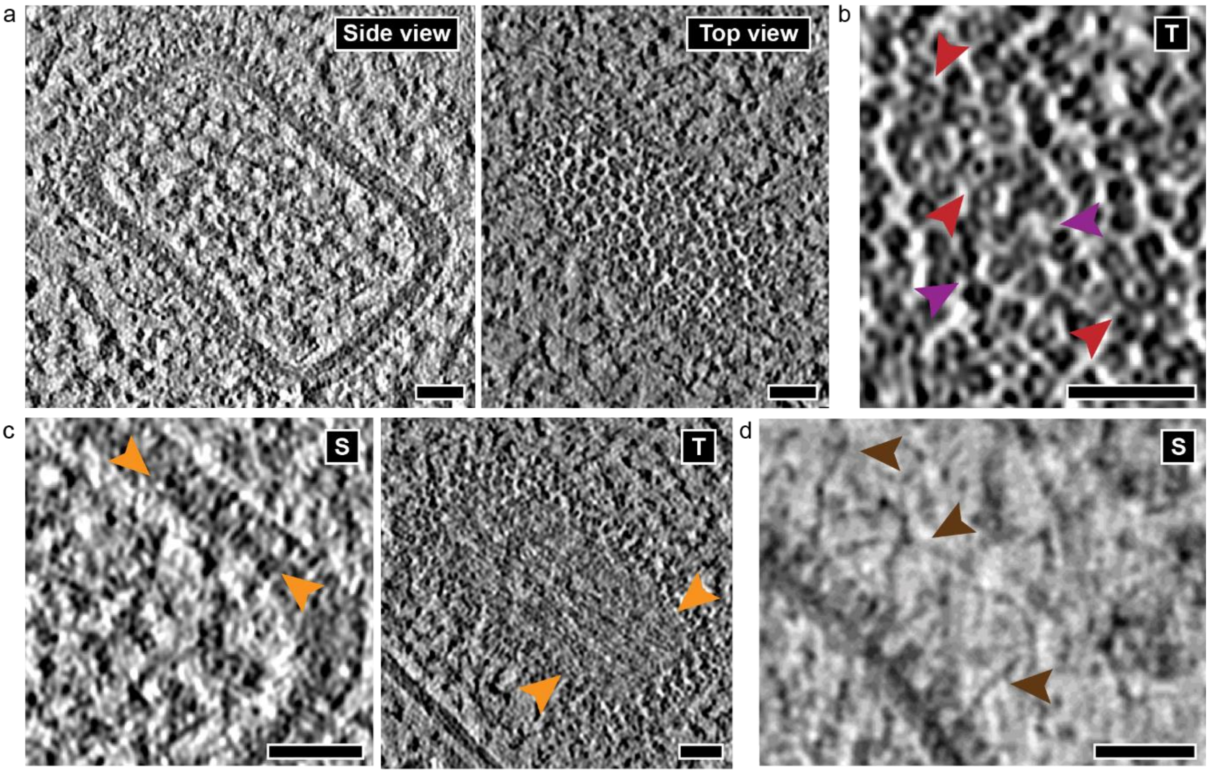

Figure 3: Analysis of incoming cores in the cytoplasm shortly after entry of Vaccinia virus into HeLa cells. Slices through a representative tomogram from a core observed in the cytoplasm early in infection show a similar architecture as cores prepared *in vitro*. (a) Slice from a middle plane of the core (side view) and from the top (top view). The most inner layer observed on *in vitro* cores is missing and filaments without clear organization, potentially the viral dsDNA genome, can be observed. (b) Close-up of the top view from the palisade layer. Similar to *in vitro* cores, there is no regular arrangement of the stakes and the thin threads connecting the stakes can be observed (violet arrowheads). The red arrowheads point to the ring-like structures. (c) Side (S) and top (T) view of the core wall with the stripes indicated by the orange arrowheads. (d) Strands observed at the surface of the palisade (brown arrowheads). Scale bars, 30 nm.

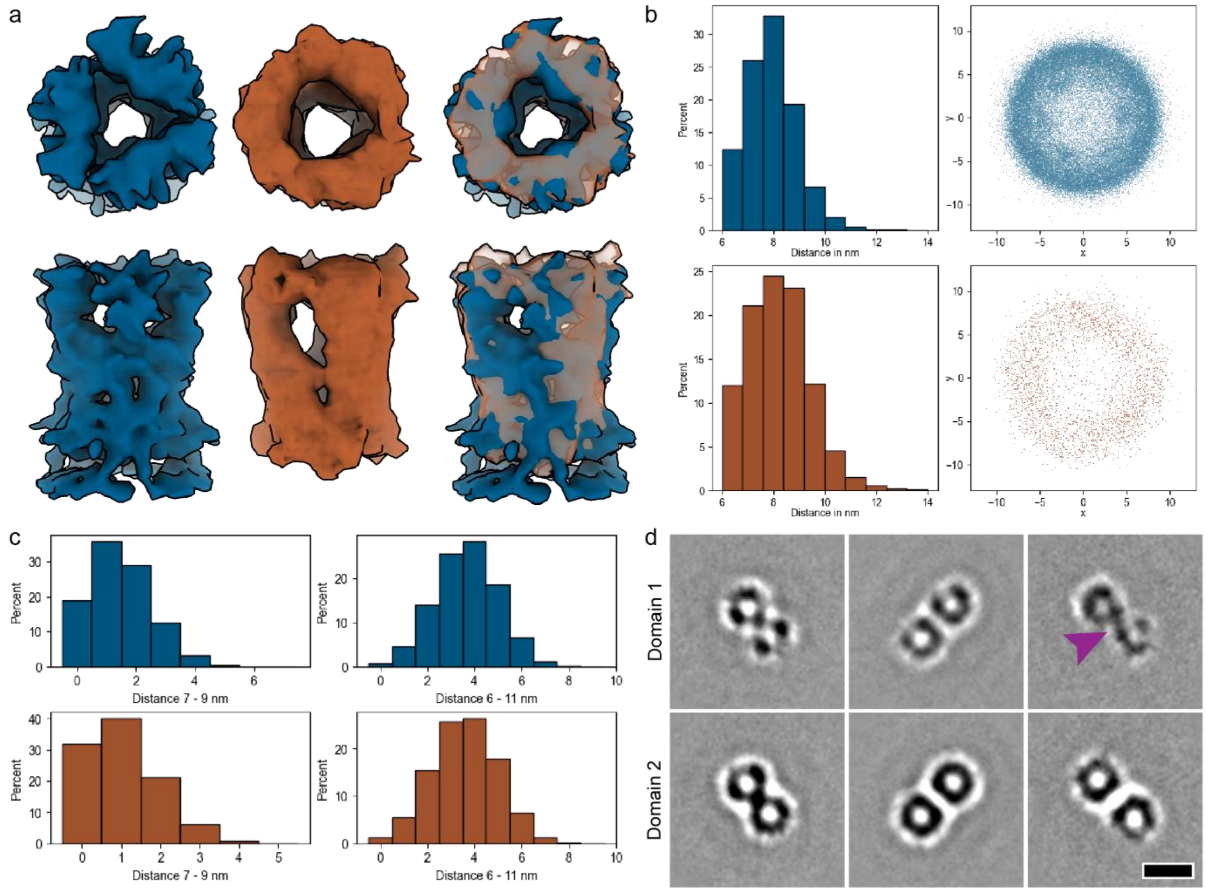

Figure 4: Comparison of *in vitro* and *in situ* palisade stakes. (a) The structures of *in vitro* (left, blue) and *in situ* (middle, brown) after localization and alignment (prior to classification). The right image shows their overlay. While the *in situ* map is less resolved (due to low number of particles and their large flexibility), the overall shape and size of both structures match very well. (b) Results of the nearest neighbor (NN) analysis performed on the trimers with top row being *in vitro* dataset and bottom row the *in situ* dataset. The histograms (right) show the average distances among the nearest neighbors, showing similar trend for both datasets. The relative position of the nearest neighbor to the normalized position and orientation of each stake is shown the right graphs. The positions are shown in 2D for xy dimension, which corresponds to the top view of the map. Although minor clustering, corresponding to the hexagonal arrangement, can be observed in the *in vitro* dataset, the majority of stakes do not form any regular arrangements. (c) Distribution of number of NN with the distance constrained to the range of 7 nm to 9 nm (left) and the whole range, i.e. 6 nm to 11 nm (right). The constrained range corresponds to the average distance between stakes ±1 nm. At this distance the stakes have predominantly only 1 to 2 neighbors for both datasets. The whole range of distance is needed to obtained more NN and even in this case the majority of stakes has 3 to 4 NN. (d) STA maps of nearest neighbor pairs at distances 6.5 nm to 7.5 nm (left), 7.5 to 8.5 nm (middle) and 8.5 to 9.5 nm (right) from the *in vitro* dataset. The top row shows cross section from the top part of the domain 1, the bottom row is the cross section from the domain 2. Despite narrow distance ranges, the stakes do not have a form of trimer as this shape was averaged out due to lack of strong preferred orientation among the pairs. At the distance from 8.5 to 9.5 nm a strong density connects the pair of stakes at the top of domain 1 (violet arrowhead) which correspond to the observed threads from Fig 1. Scale bar 10 nm.

protein	Uniprot ID	plddts
A3	P06440	79.7
A4	P29191	51.7
A10	P16715	86.1
L4	P03295	90.1
f17	P07396	71.8

Supplementary Table 1.1. List of the proteins of Vaccinia virus analyzed in this study. The average per-residue confidence score (pLDDT) is given for the highest ranked model for the different proteins, along with their corresponding Uniprot IDs. The pLDDT is the confidence measure of AlphaFold2. The score ranges from 100 (indicating perfect confidence) to 0 (indicating no confidence).

protein	oligomer	iptm+ptm
A4	dimer	0.224
	trimer	0.283
	tetramer	0.241
	pentamer	0.175
	hexamer	0.188
A3	dimer	0.761
	trimer	0.289
	tetramer	0.414
	pentamer	0.355
A10	trimer	0.823
L4	dimer	0.700
	trimer	0.163
	tetramer	0.152
	pentamer	0.167
	hexamer	0.167
f17	dimer	0.266
	trimer	0.186

Supplementary Table 1.2. List of the model score from the AlphaFold multimer software for the highest ranked model of proteins listed in Table 1.1 when different symmetries are applied. the score represents the confidence of the protein-protein interface prediction. It is calculated using the Interface pTM (iptm) score and pTM score. The score ranges from 100 (indicating perfect confidence) to 0 (indicating no confidence).

protein	iptm+ptm
A10+A3+A4	0.385
A10+A4	0.675
A3+A4+L4	0.321
A10 trimer + L4 trimer	0.562
A10 trimer + A3 dimer	0.474
A10 trimer + A4	0.696

Supplementary Table 1.3. List of the model score from the AlphaFold 2 multimer software for proteins listed in Table 1.1 in different combinations.

Step	Software	Parameters	
Image acquisition	SerialEM [38]		
CTF Estimation	CTFFind4 v.4.1.13 [20]	Pixel size	1.56 Å
		Acceleration voltage	300 keV
		Spherical aberration	2.7 mm
		Amplitude contrast	0.07
		Power spectrum size	512 pixels
		Minimum resolution	30 Å
		Maximum resolution	5 Å
		Minimum defocus	10000 Å
		Maximum defocus	75000 Å
		Defocus step	500 Å
		Astigmatism	100
Dose-exposure correction	Matlab script [21]		
High-peaks removal	eTomo v.4.10.51 (ccderaser) [39]	Peak criterion	10
		Difference criterion	8
		Maximum radius	4.2
		Extra-large difference criterion	19
Cross-correlation alignment	eTomo (tiltxcorr)	Default parameters	
Fiducial model generation	eTomo using “Make seed and track” option		
	Seed model (autofidseed)	Default parameters	
	Track beads (beadtrack)	Sobel filter	0.12 – 0.3
		Fill seed model gaps	True
		Local tracking	True
		Local area size	1000
Alignment transformation computation	eTomo (tiltalign)	Do not sort fiducial into 2 surfaces	True
		Rotation solution type	One rotation
		Magnification solution type	Fixed at 1.0
		Tilt angle solution type	Fixed
		Distortion solution type	Disabled
		Beam tilt	No
Preliminary 8x binned reconstruction	eTomo (tilt)	Logarithm of densities	No
		Radial filtering cutoff	No
		Radial filtering falloff	No
		SIRT-like filter	15 iterations
Reconstruction	novaCTF [22]	Correction type	Phaseflip
		Astigmatism correction	True
		Slab size	15 nm
Binning	Fourier3D [23]		
Core picking	Napari [40]		

Subtomogram Averaging	novaSTA [24] STOPGAP (SG)	See the table below	
FSC	STOPGAP		
Systematic Fitting	UCSF Chimera [31] together with scripts within Assembline [32]	Resolution Calpha atoms only Backbone atoms only Move PDB to center Placement number	4 False False True 10000
Flexible Fitting	Namdinator [34]	See the methods section	

SA parameters (*in vitro*)	**Manual picking (novaSTA)**	**8x binned with manual ref (novaSTA)**	**2x binned with AF2 ref (SG)**	**2x binned *de novo* (SG)**
Box size (voxels)	48	48	96	96
Iterations	10	5	1	7
Cone angle increment (degrees)	4	4	4	6 3 3 2 2 2 2
Cone angle iterations	12	12	12	4 3 3 3 1 1 2
In-plane angle increment (degrees)	6	6	12	12 12 6 3 30 10 5
In-plane angle iteration	4	4	5	5 5 5 5 6 6 6
Low-pass filter (voxels)	20	20	20	12 24 24 30 32 34 34
High-pass filter (voxels)	1	1	1	1 1 1 1 1 1 1

SA parameters (*in situ*)	**2x binned with AF2 ref (novaSTA)**	**2x binned *de novo* (SG)**
Box size (pixels)	96	56
Iterations	1	10
Cone angle increment (degrees)	4	6 3 3 2 2 2 2 2
Cone angle iterations	12	4 3 3 3 1 1 2 2
In-plane angle increment (degrees)	12	12 12 6 3 30 10 5 5
In-plane angle iteration	5	5 5 5 5 6 6 6 12
Low-pass filter (pixels)	30	12 14 14 18 18 22 22 22
High-pass filter (pixels)	1	1 1 1 1 1 1 1 1

Supplementary Table 2. Overview of software and parameters used for processing.

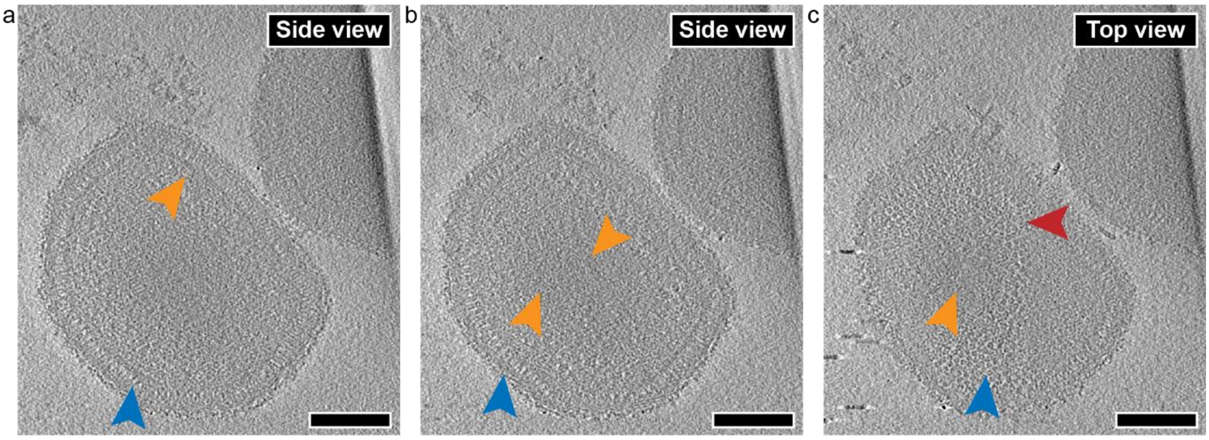

Supplementary Figure 1: Slices of a tomogram of purified mature virion (MV) of Vaccinia virus. (a) Slice of a tomogram (Movie S1) showing a cross-section of a MV with the core wall (orange arrowhead) underneath the viral envelope. Yellow arrowheads show side views of the palisade layer. (b) slice with the middle layer appearing as stripes (orange arrowheads). (c) slice closer to the top of the MV showing a top view of the palisade and the ring-like structures (red circle). Scale bars, 100 nm.

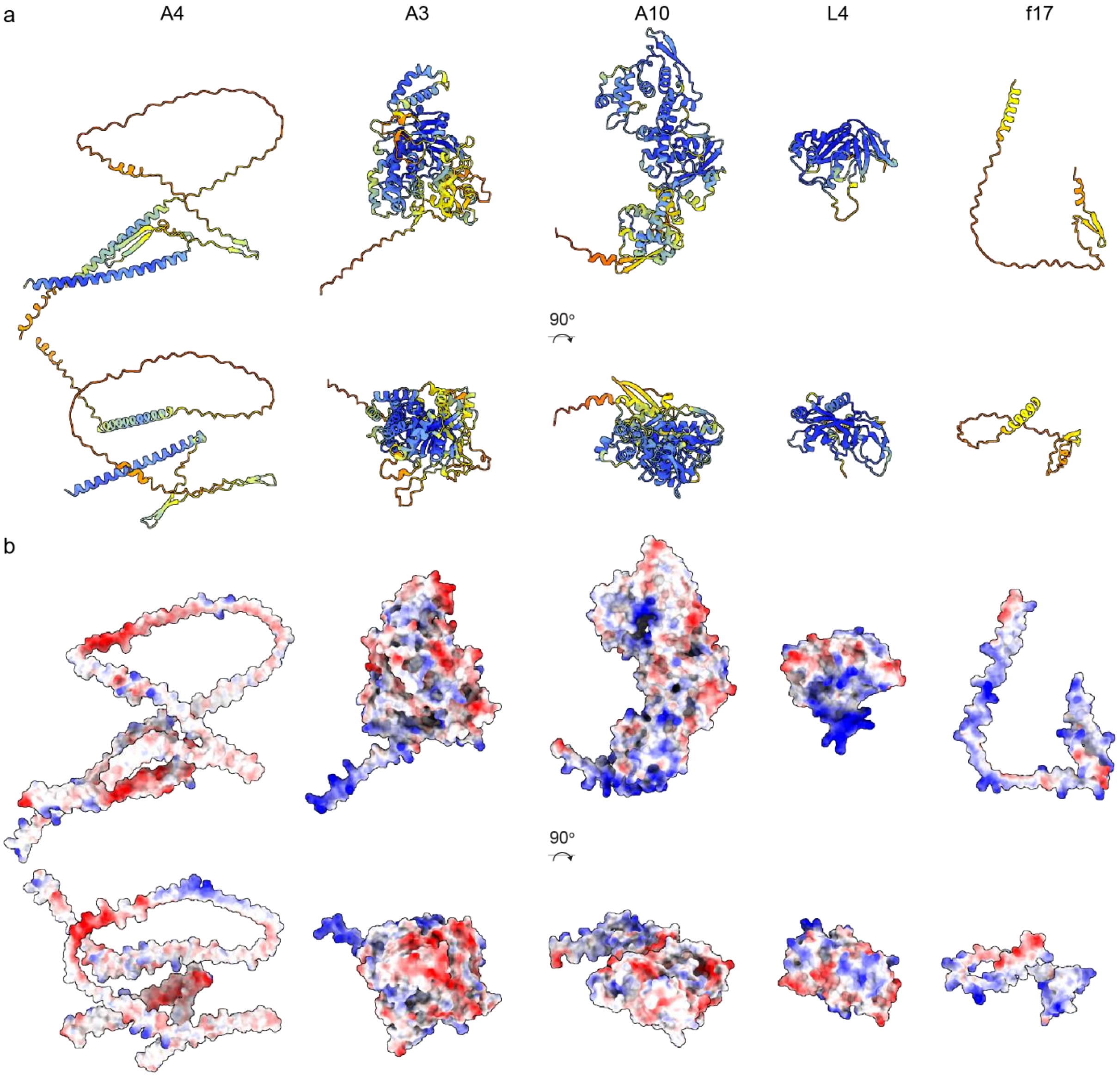

Supplementary Figure 2: Structures of monomers predicted with AlphaFold2 software. The best model predicted for A4, A3, A10, L4 and F17, is depicted (a) colored according to plddts scores. (b) electrostatic surface potentials are colored red and blue for negative and positive charges, respectively, and white color represents neutral residues.

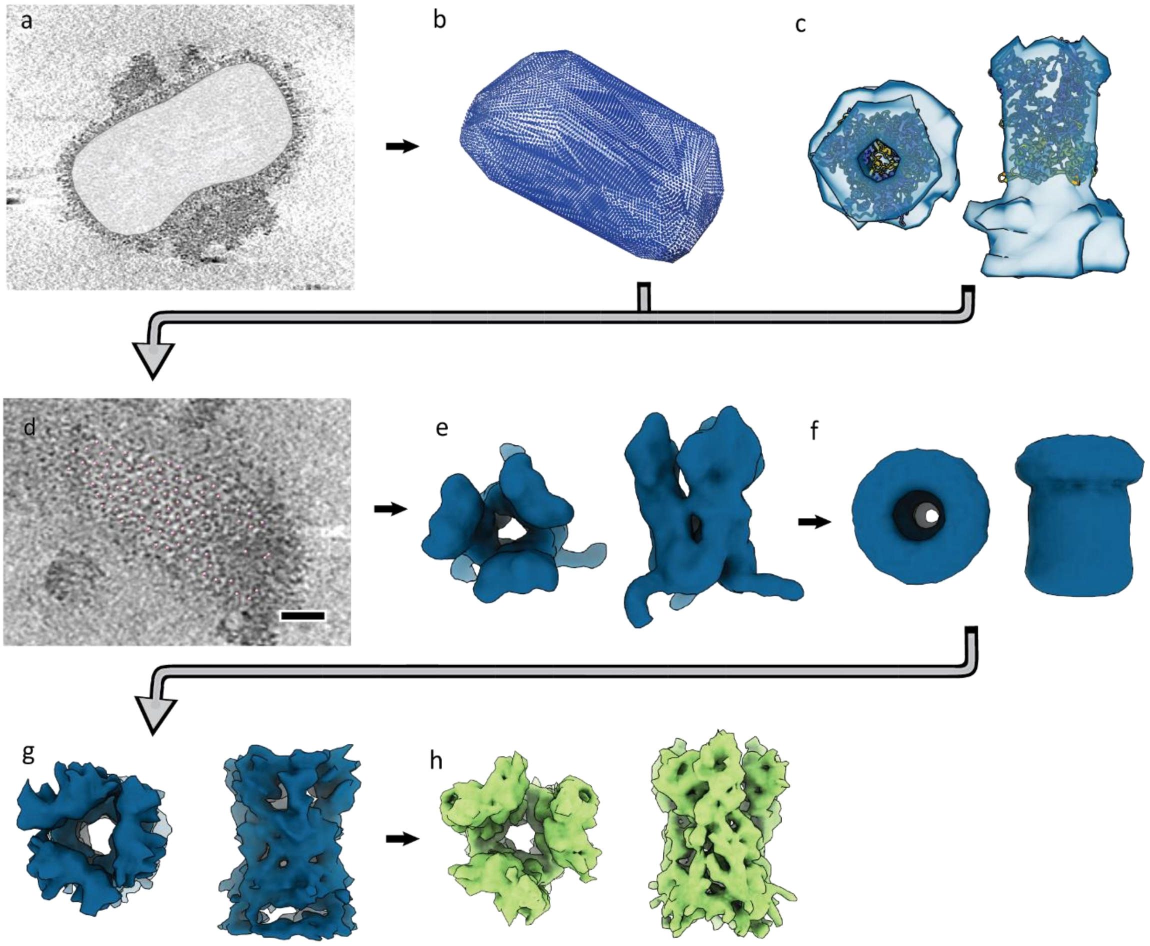

Supplementary Figure 3: Particle picking and subtomogram averaging workflow. (a) Contour layer of the core in Napari. (b) Oversampled positions on the core surface. (c) The map generated by subtomogram averaging (STA) after manual picking of the stakes with the AlphaFold2 (AF2) prediction model fitted inside using Chimera. (d) The locking of the subtomograms onto the correct positions using the AF2 prediction model as the initial reference. (e) The STA map generated using the AF2 prediction model as the reference. (f) The STA map obtained after assigning new orientations based on their position on the core surface. (g) The *de novo* STA map generated from the new surface-based orientations. (h) Loose A10 trimer produced after the classification in STOPGAP.

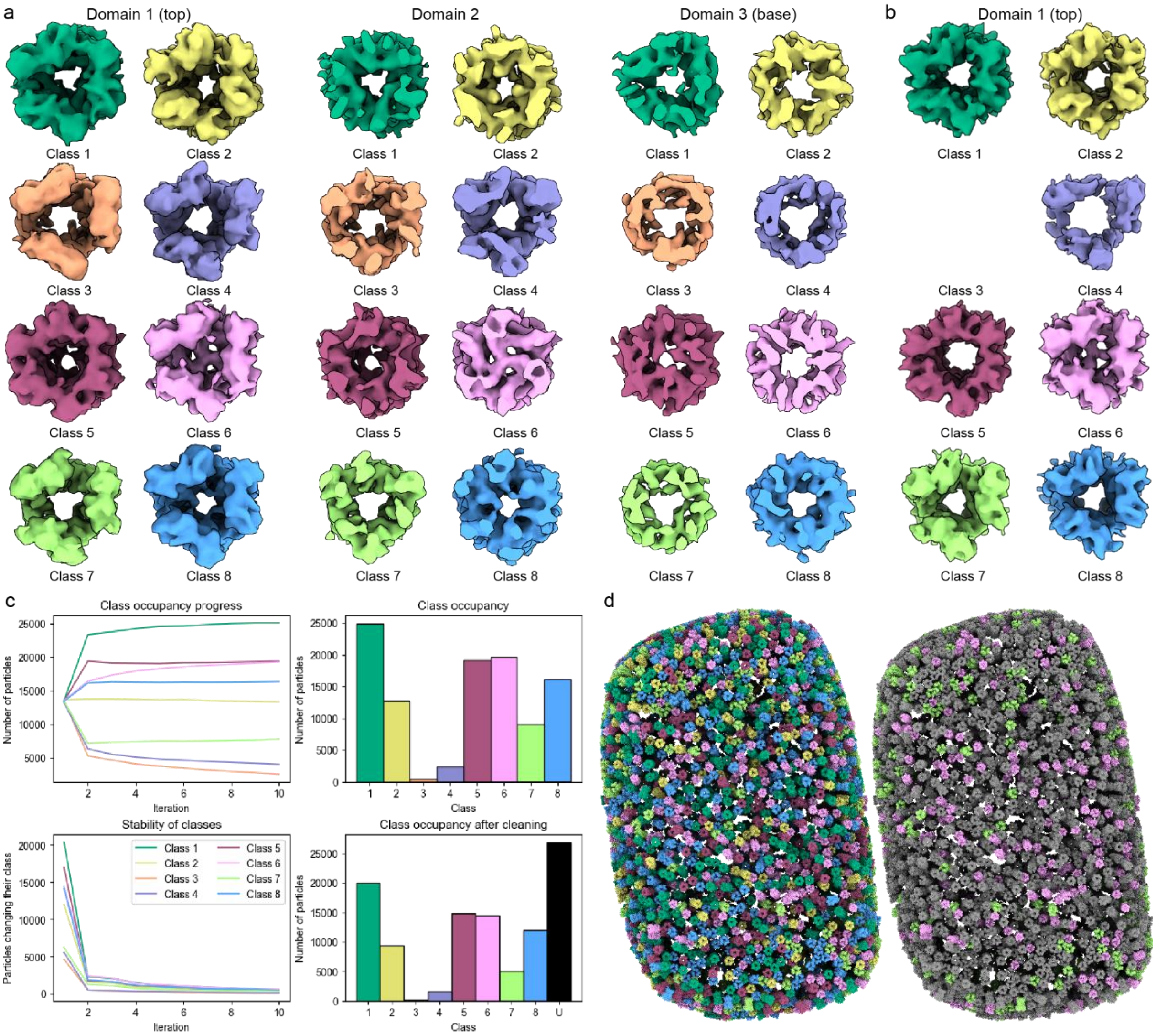

Supplementary Figure 4: Classification of subtomogram average of stalks of the palisade made of A10 trimer. (a) The classification with the starting references that were created by random subsets of particles yielded 8 different classes. The differences were mostly in the additional densities in the domain 2 (class 2, 4, 6) and domain 3 (class 1, 3, 5, 8). (b) The final 8 classes produced by 4 independent STA runs with the classes from (a) used as starting references. (c) Graphs showing class occupancy progress (top) and particle stability (bottom left) from a single STA run with the starting references from (a). Four independent and random STA runs were done and only particles that ended up in the same class for all 4 runs were kept (bottom right). The rest remained unassigned (U). (d) The final maps were plotted back to tomograms using ArtiaX plugin in ChimeraX. The color-coding corresponds to the individual classes (left panel) or classes 6 (tight trimer) and 7 only (loose trimer) (right panel). There is no apparent clustering or preferred position on the core palisade that would correspond to the assigned classes.

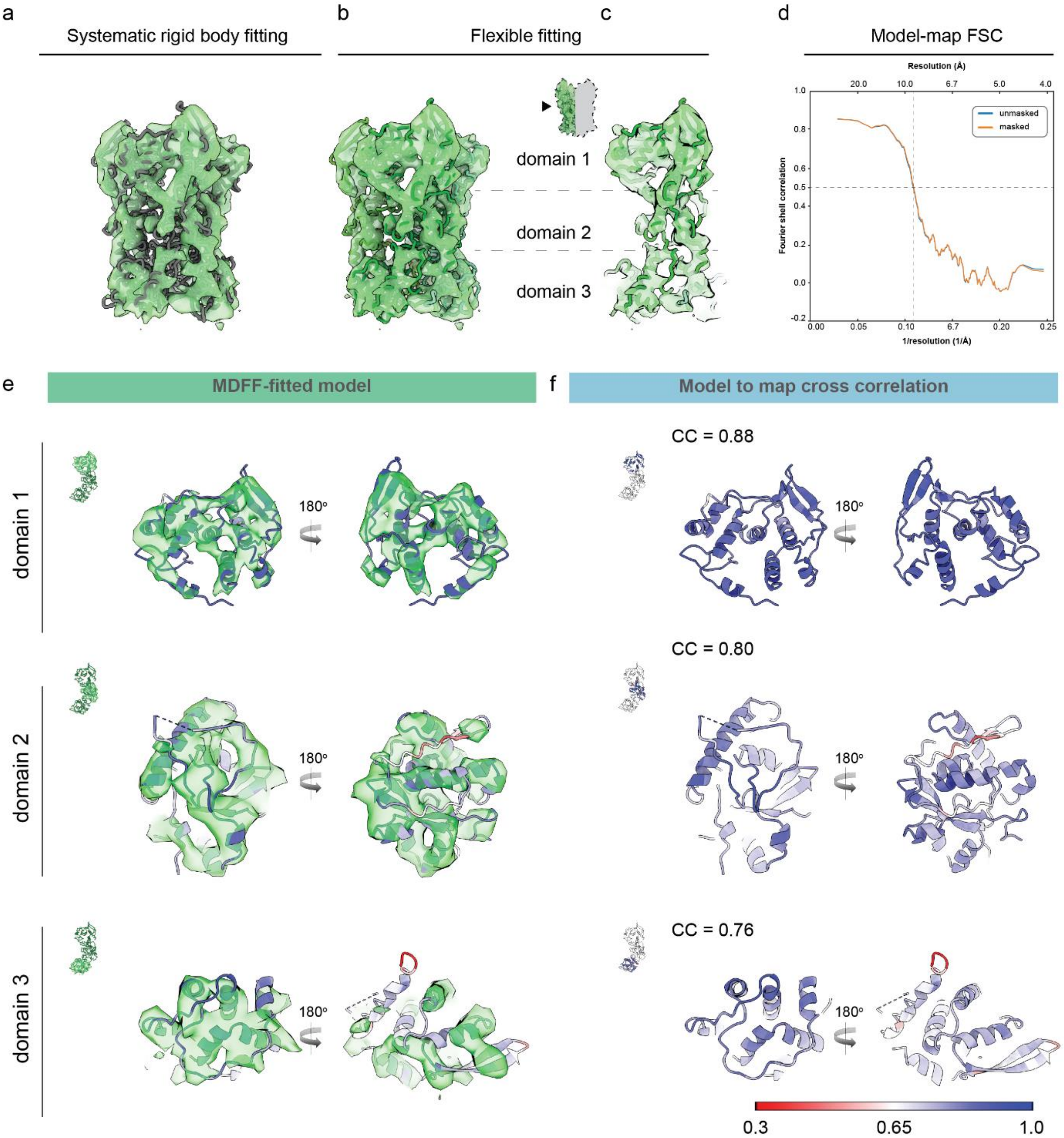

Supplementary Figure 5: A10 trimer model fitting and validation. (a) The model of an AF-predicted A10 trimer (dark grey) after systematic rigid body fitting into the cryoET density of a hollow trimer (green). (b) The model of an A10 trimer (dark green) after molecular dynamics flexible fitting (MDFF) into the cryoET density of a hollow trimer (green). The model from panel (a) was used as an initial template. (c) Clipped view of panel (b) showing the model fit of one protomer. (d) The model-map Fourier shell correlation (FSC) calculated for the model of one protomer shown in panel (c). (e) Per domain representation of the protomer fitting into cryoET density of a hollow trimer. Solvent view is shown on the left, interface view is shown on the right. (f) Per domain representation of the protomer (same as in (e) with residues colored according to the model-to-map cross-correlation (CC) scores calculated in phenix cryoEM validation tool, from the lowest (red) to highest (blue). Solvent view is shown on the left, interface view is shown on the right. The average CC scores for each domain is indicated in the upper left corner.

Supplementary movie 1: Tomogram of MV core.
Supplementary movie 2: Tomogram of two *in vitro* cores.
Supplementary movie 3: Tomogram of *in situ* core.

References:

[1] B. Moss, ‘Poxvirus membrane biogenesis’, *Virology*, vol. 479–480, pp. 619–626, May 2015, doi: 10.1016/j.virol.2015.02.003.

[2] R. C. Condit, N. Moussatche, and P. Traktman, ‘In A Nutshell: Structure and Assembly of the Vaccinia Virion’, in *Advances in Virus Research*, Academic Press, 2006, pp. 31–124. doi: 10.1016/S0065-3527(06)66002-8.

[3] M. Cyrklaff *et al.*, ‘Cryo-electron tomography of vaccinia virus’, *Proc. Natl. Acad. Sci.*, vol. 102, no. 8, pp. 2772–2777, Feb. 2005, doi: 10.1073/pnas.0409825102.

[4] O. N. Jensen *et al.*, ‘Identification of the major membrane and core proteins of vaccinia virus by two-dimensional electrophoresis’, *J. Virol.*, vol. 70, no. 11, pp. 7485–7497, Nov. 1996, doi: 10.1128/jvi.70.11.7485-7497.1996.

[5] K. Pedersen, E. J. Snijder, S. Schleich, N. Roos, G. Griffiths, and J. K. Locker, ‘Characterization of Vaccinia Virus Intracellular Cores: Implications for Viral Uncoating and Core Structure’, *J. Virol.*, vol. 74, no. 8, pp. 3525–3536, Apr. 2000, doi: 10.1128/JVI.74.8.3525-3536.2000.

[6] K. B. Easterbrook, ‘Controlled degradation of vaccinia virions in vitro: an electron microscopic study’, *J. Ultrastruct. Res.*, vol. 14, no. 5, pp. 484–496, Mar. 1966, doi: 10.1016/S0022-5320(66)80077-1.

[7] S. Wilton, A. R. Mohandas, and S. Dales, ‘Organization of the Vaccinia Envelope and Relationship to the Structure of Intracellular Mature Virions’, *Virology*, vol. 214, no. 2, pp. 503–511, Dec. 1995, doi: 10.1006/viro.1995.0061.

[8] J. Dubochet, M. Adrian, K. Richter, J. Garces, and R. Wittek, ‘Structure of intracellular mature vaccinia virus observed by cryoelectron microscopy’, *J. Virol.*, vol. 68, no. 3, pp. 1935–1941, Mar. 1994, doi: 10.1128/jvi.68.3.1935-1941.1994.

[9] M. Hernandez-Gonzalez, T. Calcraft, A. Nans, P. B. Rosenthal, and M. Way, ‘A succession of two viral lattices drives vaccinia virus assembly’, *PLoS Biol.*, vol. 21, no. 3, p. e3002005, Mar. 2023, doi: 10.1371/journal.pbio.3002005.

[10] J. Jumper *et al.*, ‘Highly accurate protein structure prediction with AlphaFold’, *Nature*, vol. 596, no. 7873, Art. no. 7873, Aug. 2021, doi: 10.1038/s41586-021-03819-2.

[11] B. Moss, B. Y. Ahn, B. Amegadzie, P. D. Gershon, and J. G. Keck, ‘Cytoplasmic transcription system encoded by vaccinia virus’, *J. Biol. Chem.*, vol. 266, no. 3, pp. 1355–1358, Jan. 1991, doi: 10.1016/S0021-9258(18)52298-5.

[12] M. Cyrklaff *et al.*, ‘Whole Cell Cryo-Electron Tomography Reveals Distinct Disassembly Intermediates of Vaccinia Virus’, *PLOS ONE*, vol. 2, no. 5, p. e420, May 2007, doi: 10.1371/journal.pone.0000420.

[13] F. I. Schmidt *et al.*, ‘Vaccinia virus entry is followed by core activation and proteasome-mediated release of the immunomodulatory effector VH1 from lateral bodies’, *Cell Rep.*, vol. 4, no. 3, pp. 464–476, Aug. 2013, doi: 10.1016/j.celrep.2013.06.028.

[14] D. Rodriguez *et al.*, ‘A vaccinia virus lacking A10L: viral core proteins accumulate on structures derived from the endoplasmic reticulum’, *Cell. Microbiol.*, vol. 8, no. 3, pp. 427–437, 2006, doi: 10.1111/j.1462-5822.2005.00632.x.

[15] E. Katz and B. Moss, ‘Vaccinia virus structural polypeptide derived from a high-molecular-weight precursor: formation and integration into virus particles’, *J. Virol.*, vol. 6, no. 6, pp. 717–726, Dec. 1970, doi: 10.1128/JVI.6.6.717-726.1970.

[16] C.-S. Chung, C.-H. Chen, M.-Y. Ho, C.-Y. Huang, C.-L. Liao, and W. Chang, ‘Vaccinia Virus Proteome: Identification of Proteins in Vaccinia Virus Intracellular Mature Virion

Particles', *J. Virol.*, vol. 80, no. 5, pp. 2127–2140, Mar. 2006, doi: 10.1128/JVI.80.5.2127-2140.2006.
[17] M. Mallardo, S. Schleich, and J. Krijnse Locker, 'Microtubule-dependent Organization of Vaccinia Virus Core–derivd Early mRNAs into Distinct Cytoplasmic Structures', *Mol. Biol. Cell*, vol. 12, no. 12, pp. 3875–3891, Dec. 2001, doi: 10.1091/mbc.12.12.3875.
[18] W. J. H. Hagen, W. Wan, and J. A. G. Briggs, 'Implementation of a cryo-electron tomography tilt-scheme optimized for high resolution subtomogram averaging', *J. Struct. Biol.*, vol. 197, no. 2, pp. 191–198, Feb. 2017, doi: 10.1016/j.jsb.2016.06.007.
[19] B. Turoňová *et al.*, 'Benchmarking tomographic acquisition schemes for high-resolution structural biology', *Nat. Commun.*, vol. 11, no. 1, p. 876, Feb. 2020, doi: 10.1038/s41467-020-14535-2.
[20] A. Rohou and N. Grigorieff, 'CTFFIND4: Fast and accurate defocus estimation from electron micrographs', *J. Struct. Biol.*, vol. 192, no. 2, pp. 216–221, Nov. 2015, doi: 10.1016/j.jsb.2015.08.008.
[21] W. Wan *et al.*, 'Structure and assembly of the Ebola virus nucleocapsid', *Nature*, vol. 551, no. 7680, pp. 394–397, Nov. 2017, doi: 10.1038/nature24490.
[22] B. Turoňová, F. K. M. Schur, W. Wan, and J. A. G. Briggs, 'Efficient 3D-CTF correction for cryo-electron tomography using NovaCTF improves subtomogram averaging resolution to 3.4Å', *J. Struct. Biol.*, vol. 199, no. 3, pp. 187–195, Sep. 2017, doi: 10.1016/j.jsb.2017.07.007.
[23] turonova, 'turonova/Fourier3D: Fourier3D'. Zenodo, Aug. 05, 2020. doi: 10.5281/zenodo.3973621.
[24] turonova, 'turonova/novaSTA: novaSTA'. Zenodo, Aug. 05, 2020. doi: 10.5281/zenodo.3973623.
[25] R. Evans *et al.*, 'Protein complex prediction with AlphaFold-Multimer'. bioRxiv, p. 2021.10.04.463034, Mar. 10, 2022. doi: 10.1101/2021.10.04.463034.
[26] W. Wan, S. Khavnekar, J. Wagner, P. Erdmann, and W. Baumeister, 'STOPGAP: A Software Package for Subtomogram Averaging and Refinement', *Microsc. Microanal.*, vol. 26, no. S2, pp. 2516–2516, Aug. 2020, doi: 10.1017/S143192762002187X.
[27] B. Turoňová *et al.*, 'In situ structural analysis of SARS-CoV-2 spike reveals flexibility mediated by three hinges', *Science*, vol. 370, no. 6513, pp. 203–208, Oct. 2020, doi: 10.1126/science.abd5223.
[28] U. H. Ermel, S. M. Arghittu, and A. S. Frangakis, 'ArtiaX: An Electron Tomography Toolbox for the Interactive Handling of Sub-Tomograms in UCSF ChimeraX'. bioRxiv, p. 2022.07.26.501574, Jul. 27, 2022. doi: 10.1101/2022.07.26.501574.
[29] E. F. Pettersen *et al.*, 'UCSF ChimeraX: Structure visualization for researchers, educators, and developers', *Protein Sci.*, vol. 30, no. 1, pp. 70–82, 2021, doi: 10.1002/pro.3943.
[30] C. E. Zimmerli *et al.*, 'Nuclear pores dilate and constrict in cellulo', *Science*, vol. 374, no. 6573, p. eabd9776, Dec. 2021, doi: 10.1126/science.abd9776.
[31] E. F. Pettersen *et al.*, 'UCSF Chimera--a visualization system for exploratory research and analysis', *J Comput Chem*, vol. 25, no. 13, pp. 1605–1612, Oct. 2004, doi: 10.1002/jcc.20084.
[32] V. Rantos, K. Karius, and J. Kosinski, 'Integrative structural modeling of macromolecular complexes using Assembline', *Nat. Protoc.*, vol. 17, no. 1, pp. 152–176, Apr. 2022, doi: 10.1038/s41596-021-00640-z.

[33] A. P. Schuller *et al.*, 'The cellular environment shapes the nuclear pore complex architecture', *Nature*, vol. 598, no. 7882, Art. no. 7882, Oct. 2021, doi: 10.1038/s41586-021-03985-3.

[34] R. T. Kidmose, J. Juhl, P. Nissen, T. Boesen, J. L. Karlsen, and B. P. Pedersen, 'Namdinator – automatic molecular dynamics flexible fitting of structural models into cryo-EM and crystallography experimental maps', *IUCrJ*, vol. 6, no. 4, pp. 526–531, Jul. 2019, doi: 10.1107/S2052252519007619.

[35] P. V. Afonine *et al.*, 'New tools for the analysis and validation of cryo-EM maps and atomic models', *Acta Crystallogr. Sect. Struct. Biol.*, vol. 74, no. Pt 9, pp. 814–840, Sep. 2018, doi: 10.1107/S2059798318009324.

[36] G. D. Pintilie, J. Zhang, T. D. Goddard, W. Chiu, and D. C. Gossard, 'Quantitative analysis of cryo-EM density map segmentation by watershed and scale-space filtering, and fitting of structures by alignment to regions', *J. Struct. Biol.*, vol. 170, no. 3, pp. 427–438, Jun. 2010, doi: 10.1016/j.jsb.2010.03.007.

[37] M. Laguerre, M. Saux, J. P. Dubost, and A. Carpy, 'MLPP: A Program for the Calculation of Molecular Lipophilicity Potential in Proteins', *Pharm. Pharmacol. Commun.*, vol. 3, no. 5–6, pp. 217–222, 1997, doi: 10.1111/j.2042-7158.1997.tb00257.x.

[38] D. N. Mastronarde, 'Automated electron microscope tomography using robust prediction of specimen movements', *J. Struct. Biol.*, vol. 152, no. 1, pp. 36–51, Oct. 2005, doi: 10.1016/j.jsb.2005.07.007.

[39] J. R. Kremer, D. N. Mastronarde, and J. R. McIntosh, 'Computer Visualization of Three-Dimensional Image Data Using IMOD', *J. Struct. Biol.*, vol. 116, no. 1, pp. 71–76, Jan. 1996, doi: 10.1006/jsbi.1996.0013.

[40] N. Sofroniew *et al.*, 'napari: a multi-dimensional image viewer for Python'. Zenodo, Nov. 03, 2022. doi: 10.5281/zenodo.7276432.